Strain stabilization and thickness dependence of magnetism in epitaxial transition metal monosilicide thin films on Si(111)

Benjamin Geisler and Peter Kratzer
Fakultät für Physik and Center for Nanointegration (CeNIDE), Universität Duisburg-Essen, 47048 Duisburg, Germany
(Received 8 July 2013; published 26 September 2013)

We present a comprehensive study of different 3*d* transition metal monosilicides in their ground state crystal structure (B20), ranging from equilibrium bulk over biaxially strained bulk to epitaxial thin films on Si(111), by means of density functional theory. The magnetic properties of MnSi and FeSi films are found to be considerably modified due to the epitaxial strain induced by the substrate. In MnSi bulk material, which can be seen as a limit of thick films, we find a strain-induced volume expansion, an increase of the magnetic moments, and a significant rise of the energy difference between different spin configurations. The latter can be associated with an increase of the Curie temperature, which is in accordance with recent experimental results. While a ferromagnetic spin alignment is found to be the ground state also for ultrathin films, we show that for films of intermediate thickness a partially compensating magnetic ordering is more favorable; however, the films retain a net magnetic moment. Furthermore, we analyze the orbital structure in FeSi around the band gap, which can be located somewhere in the density of states for all studied B20 transition metal monosilicides, and find that FeSi becomes metallic and ferromagnetic under epitaxial strain. Finally, the influence of on-site electronic correlation and the reliability of *ab initio* calculations for 3*d* transition metal monosilicides are discussed.

DOI: 10.1103/PhysRevB.88.115433 PACS number(s): 71.15.Mb, 71.20.−b, 73.20.At, 75.70.−i

I. INTRODUCTION

The combination of semiconducting and ferromagnetic (FM) materials is of strong interest in the fields of spintronics and magnetoelectronics, since exploiting the spin degree of freedom in addition to our standard charge-based electronics would be valuable and will hopefully lead to new devices for information processing and data storage.[1,2]

For technological applications, some constraints should be kept in mind: First of all, the involved materials should be "established" in the sense that the technology for device production is either already available or that it can be integrated into existing processes. Second, the process itself should be kept as simple as possible. Hence, Si-based spintronics is an area of ongoing research since Si is the de-facto standard semiconductor and desirable from a technological as well as economical point of view. A possible way to fabricate a spin injector is by epitaxially growing a FM, metallic film (ideally with small conductivity mismatch) on top of the Si substrate. Transition metals (TMs) are an obvious choice for constructing such a heterostructure: Their abundance is good, and they are known to react strongly (exothermic) with a Si surface. So just by codeposition of TM and Si atoms on a Si surface and moderate annealing one can form magnetic silicide films of high structural and interfacial quality on top of the semiconductor.[3–5] The drawback is that such silicides in their ground state crystal structure are often non- or only weakly magnetic, even those one would expect to be promising due to the high magnetic moment of the constituents, like CrSi, MnSi, or FeSi. Also, $CrSi_2$, CoSi, $CoSi_2$, and NiSi are of no interest in this context.[6]

However, structural modifications induced by epitaxial growth can possibly improve this situation. In the last years, several theoretical studies based upon *ab initio* thermodynamical arguments concerning TM (silicide) thin films on Si have been published. The focus lay on the technologically relevant Si(100) surface, on which films of different TM monosilicides in B2 (CsCl) structure have been investigated.[7] Mn was found to be most promising.[8] Later, also thin Mn monosilicide films on the Si(111) surface were studied, comparing the B2 to the B20 structure.[9] The advantage of Si(111) is that it is compatible to both the MnSi-B20 and MnSi-B2 structures, the lattice constant fitting better to MnSi-B20. The competition between thin-film growth and island nucleation has also been discussed.[9] It was found that MnSi on Si(100) tends to form three-dimensional (3D) islands instead of thin films. The situation is better on the Si(111) surface where thin film formation is more probable since island nuclei need to be larger. The thermodynamic properties of different surface terminations of MnSi-B20 thin films grown by different epitaxial techniques on Si(111) have been discussed and conclusions about the growth conditions have been drawn by detailed comparison and analysis of simulated and experimental scanning tunneling microscopy images, considering the possible existence of two different stacking sequences.[10]

In this work we study a set of TM monosilicides in B20 structure and especially the influence of epitaxial strain on their structural, electronic, and magnetic properties by means of density functional theory, starting with a discussion of unstrained and biaxially strained bulk systems. Since the magnetism in MnSi showed the most significant response to biaxial strain in the (111) plane according to our calculations, we constructed MnSi/Si(111) thin film heterostructures of different film thickness and studied the deviations of their magnetic behavior from the aforementioned bulk case. As we will show, our results agree qualitatively with recent experimental observations for MnSi/Si(111) thin films,[3,4] which we consider to be a notable result due to the electronic correlations present in the silicides.[11,12] We also discuss experimental data recently measured for FeSi/Si(111) thin films.[5] Finally, we present results derived from an approach that includes on-site electronic correlation effects and comment on the reliability of *ab initio* calculations for such materials.

II. METHODOLOGY

We performed first-principles calculations in the framework of spin-polarized density functional theory[13] (DFT) using the QUANTUMESPRESSO code,[14] which employs plane waves as basis functions. Exchange and correlations have been described by the PBE generalized gradient approximation (GGA) functional,[15] which has been used successfully in studies of different TM silicides in the past.[7–10] Noncollinear spin configurations, as they arise for example in MnSi, have been approximated to be collinear. This is reasonable since the wavelength of MnSi spin helices, for example, is much longer than the size of our considered systems. Thus, any spin noncollinearity would just result in a small correction to the total energy.

Wave functions and density have been expanded into plane waves up to cutoff energies of 35 and 350 Ry, respectively. The neighborhood of atom centers has been approximated by self-created ultrasoft pseudopotentials (USPP),[16] treating the atomic Si $3s$, $3p$ and TM $3p$, $3d$, $4s$, $4p$ subshells as valence states.[17] Ti had an additional $3s$ orbital. For Si, Cr, Mn, and Fe a nonlinear core correction[18] was included. Bulk calculations of B20 TM silicides were carried out using simple cubic unit cells with eight atoms. In [111] direction, a rhombohedral unit cell (as used by Ref. 19) comprising eight atoms does not allow for more complex magnetic configurations than ferromagnetism. Thus, we used a hexagonal cell with 24 atoms (12 formula units, f.u.) for our strained-bulk calculations. The transformation from the simple cubic cell to a hexagonal cell can be seen in Fig. 1.

For the thin film structures we used a supercell approach: A hexagonal Si(111)-($\sqrt{3}\times\sqrt{3}$) unit cell containing six layers of Si, the MnSi films, and a vacuum region of about 20 Å was used.[10] The lower side of the Si substrate was passivated by H atoms. The lateral cell size was fixed to the calculated Si(111)-($\sqrt{3}\times\sqrt{3}$) surface lattice constant. A dipole correction scheme[20,21] was included, but found to be of minor importance.

Brillouin zone sampling was done using Methfessel-Paxton smearing[22] (5 mRy) and different Monkhorst-Pack k-point grids,[23] depending on the problem: For the bulk calculations we used a $16\times16\times16$ grid for cubic unit cells, and a $6\times6\times4$ grid for hexagonal unit cells. Furthermore, we used a $4\times4\times1$ grid for the FM thin film structures. For other magnetic configurations, a $6\times6\times1$ grid proved to be more reliable for achieving self-consistency; the energy differences to the $4\times4\times1$ grid, however, have been found to be negligible. All grids were chosen in such a way that they did not include the Γ point. For densities of states, the post-processing was performed with denser k-point grids that included the Γ point.

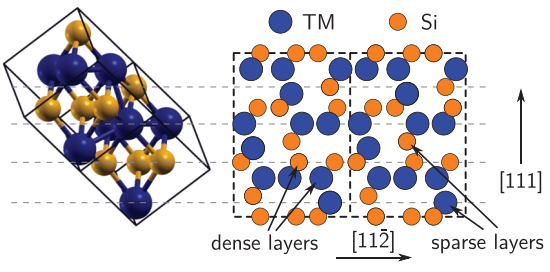

FIG. 1. (Color online) Two simple cubic unit cells (left) showing the B20 structure and the buildup of the dense and sparse layers in [111] direction. The hexagonal cell (indicated to the right) contains 24 atoms and repeats after 12 layers in [111] direction. Small orange (big blue) spheres depict Si (TM) atoms.

All internal atomic positions were accurately optimized using Hellmann-Feynman forces to reduce the force components below 1 mRy/bohr and the energy changes below 0.1 mRy.

Constrained total moment calculations were carried out using two separate Fermi energies, one for each spin channel.

For testing purposes, all-electron calculations were performed using the full-potential linearized augmented plane-wave plus local-orbital (LAPW) technique.[24] We used muffin-tin radii of 1.06–1.11 Å for both the TM and Si atoms, an interstitial plane wave cutoff of $E_{\mathrm{cut}}^{\mathrm{WF}}=20$ Ry, and wave function and density expansions up to $l_{\mathrm{max}}^{\mathrm{WF}}=12$ and $G_{\mathrm{max}}=14$.

III. BULK PROPERTIES OF DIFFERENT TRANSITION METAL MONOSILICIDES

A. Structural aspects

The B20 structure of TM monosilicides, which is the ground state crystal structure for CrSi, MnSi, FeSi, and CoSi, can be described by a simple cubic unit cell containing four TM and four Si atoms sitting on $4a$ Wyckoff positions (Fig. 1). The space group is $P2_13$. The Wyckoff positions are (u_x,u_x,u_x), $(-u_x+\frac{1}{2},-u_x,u_x+\frac{1}{2})$, $(-u_x,u_x+\frac{1}{2},-u_x+\frac{1}{2})$, $(u_x+\frac{1}{2},-u_x+\frac{1}{2},-u_x)$, $x\in\{\mathrm{TM,Si}\}$, so different values for u have to be used for TM and Si atoms.

Table I shows our calculated lattice constants for all considered bulk TM-Si compounds and compares them to recently calculated values using the projector augmented wave method and the PW91 exchange-correlation functional[25] as well as to experimental values.[26,27] One can see that the agreement with Ref. 25 is almost perfect, especially when keeping in mind that different exchange-correlation functionals have been used. Compared to experimental values, our DFT-PBE lattice constants for CrSi, MnSi, FeSi, and CoSi are underestimated by only −0.8%, −0.9%, −1.1%, and −0.4%, which is also very good. Additionally, we performed all-electron LAPW calculations to get an impression of the deviations caused by the pseudopotential approach and found them to be small

TABLE I. Lattice constants of different, completely relaxed materials in B20 structure compared to literature. $M_{\mathrm{calc}}^{\mathrm{PBE}}$ denotes the total magnetic moment per f.u. The magnetic moments localized at the TM atoms are given in parentheses.

	$a_{\mathrm{calc}}^{\mathrm{PBE}}$ (Å)	$a_{\mathrm{calc}}^{\mathrm{PW91}}$ (Å)[a]	a_{expt} (Å)[b]	$M_{\mathrm{calc}}^{\mathrm{PBE}}$ (μ_{B})
TiSi	4.972	–	–	0.00 (0.00)
VSi	4.735	4.739	–	0.00 (0.00)
CrSi	4.590	4.600	4.629	0.41 (0.45)
MnSi	4.516	4.519	4.558	1.00 (1.11)
FeSi	4.445	4.448	4.493	0.00 (0.00)
CoSi	4.430	4.442	4.447	0.00 (0.00)
NiSi	4.515	4.535	–	0.00 (0.00)

[a]Reference 25.
[b]References 26 and 27.

TABLE II. Calculated bulk modulus $B_{\mathrm{calc}}^{\mathrm{PBE}}$ and Wyckoff parameters u for TM and Si atoms of different materials in B20 structure. In parentheses, experimental values are shown (Ref. 26).

	$B_{\mathrm{calc}}^{\mathrm{PBE}}$ (GPa)	$u_{\mathrm{calc}}^{\mathrm{TM}}$	$1-u_{\mathrm{calc}}^{\mathrm{Si}}$
TiSi	131	0.143	0.156
VSi	176	0.139	0.153
CrSi	188	0.137 (0.136)	0.152 (0.154)
MnSi	208	0.137 (0.138)	0.155 (0.154)
FeSi	215	0.136 (0.136)	0.160 (0.156)
CoSi	214	0.145 (0.14?)	0.157 (0.16?)
NiSi	173	0.149	0.154

(cf. Tables I and II). For MnSi we get a very good agreement of the lattice constant (4.53 Å) and the bulk modulus (204 GPa).[10] The results for FeSi (4.46 Å, 228 GPa) and CrSi (4.60 Å, 187 GPa) are also good.

The equilibrium lattice constant is maximal for TiSi, reducing continuously until CoSi, and going up again for NiSi. The bulk modulus increases from TiSi to FeSi and CoSi, reducing again for NiSi. We determined the Wyckoff positions u_{TM} and u_{Si} for each compound for several values of the lattice constant from optimizations of the internal structural parameters (not shown). Two trends can be deduced: First, u_{TM} tends to decrease as the lattice constant becomes larger, while $1-u_{\mathrm{Si}}$ increases. Second, this trend becomes more pronounced with increasing valency.

The "ideal" B20 structure is characterized by $u_{\mathrm{TM}} = 1/(4\tau) \approx 0.155$ and $u_{\mathrm{Si}} = 1 - 1/(4\tau) \approx 0.845$, where $\tau = (1+\sqrt{5})/2$ is the golden ratio.[28,29] In this case, the inversion operation interchanges the TM and Si sites (by construction) since $u_{\mathrm{TM}} = 1 - u_{\mathrm{Si}}$. From aforementioned structural optimizations and Table II it can be seen that in our case all u_{TM} lie well below this value for all considered lattice constants, albeit they approach it as uniform (hydrostatic) pressure is applied. This general trend has already been predicted for FeSi.[28] For MnSi, the energy difference between real and ideal B20 structure at their respective equilibrium lattice constant is 161 ± 5 meV per f.u. in our calculations. For FeSi, a value of 120 meV has been reported.[28] The deviation of the equilibrium Wyckoff parameter u_{TM} from its ideal value decreases from TiSi to FeSi, jumping up again for CoSi and NiSi (Table II).

As indicated above, the ground state crystal structure of TiSi and NiSi is actually not B20, but B27 for TiSi[30] and B31 for NiSi.[31] Both have the *Pnma* space group (like MnP). We performed full-optimization calculations (cell parameters a, b, c and internal atom coordinates) for TiSi and NiSi and found in both cases nonmagnetic (NM) solutions with an energy spacing to the B20 phase of 570 and 177 meV per f.u., respectively. For VSi we found no data in the literature, only for different stoichiometries (like VSi_2, V_3Si, V_5Si_3).[31,32]

B. Electronic and magnetic properties

Two TM-Si compounds have been discussed predominantly over the last years: MnSi and FeSi. For both, intense research is still ongoing.

MnSi as bulk material is a chiral itinerant ferromagnet. Its complex magnetic structure is well studied: Several different magnetic phases exist, including a recently observed skyrmion phase[33] and a magnetic blue phase.[34] Without external magnetic field, MnSi shows a helical magnetic order of long wavelength (175–190 Å) below the critical temperature $T_C \approx 29.5$ K.[35] This helicity can be explained by the missing inversion symmetry of the crystal lattice which results in a nonvanishing Dzyaloshinsky-Moriya (DM) term in the spin density expansion of the free energy.[36,37] If an externally applied magnetic field exceeds $\mu_0 H_{C2} \approx 300$–550 mT, the DM contributions are overcome and the spins align ferromagnetically.[33,38,39] First-principles calculations based on the local density approximation (LDA) predicted a total magnetic moment of 1 μ_B per f.u.[29] On the other hand, experiments report a saturation moment of 0.4 μ_B in the polarized phase at high external magnetic field, which strongly deviates from a moment of 2.27 μ_B according to a Curie-Weiss fit in the paramagnetic phase.[40,41]

FeSi also exhibits some special properties: Around room temperature, it shows a transition from a NM, semiconducting ground state with a narrow band gap to a metal.[42,43] The magnetic susceptibility rises exponentially up to 500 K and follows a Curie-Weiss temperature dependence at higher temperatures.[44] These unusual phenomena led to several model assumptions in the past, like FeSi being a d-electron Kondo insulator.[42,45,46] However, this view has been questioned recently by experimental[47] and theoretical[12] works which state that a correlated band insulator picture, where the $3d$ bands are renormalized due to electron-electron interactions, is more appropriate. Photoemission experiments measured a band gap width of around 60 meV at low temperatures,[48,49] while tunneling spectroscopy reported 50 meV.[42] Paschen *et al.* stated that the gap appears to be smaller in transport measurements (55–70 meV) than for charge or spin excitations (75–100 meV).[43] Early LDA calculations reported a wider gap of 130 meV.[50] The gap closes quickly with increasing temperature.[48,49] This is in agreement with recent theoretical estimates of the optical conductivity, which showed no sign of a band gap above a temperature of 386 K.[12]

From the densities of states (DOS) for the bulk compounds (Fig. 2) it becomes obvious that the TM monosilicides in B20 structure follow a similar electron filling scheme as reported for the artificial zinc-blende structure.[25] The overall shape of the DOS is always the same, like in a rigid-band model (neglecting the exchange splitting for CrSi and MnSi for the moment), but a reduction of the $3d$ bandwidth for the late TMs can be observed. The band gap, which has been studied experimentally for FeSi, can be observed somewhere in the DOS for *all* considered TM silicides and thus has to be already a consequence of the sevenfold atom coordination in the B20 crystal structure. (Note that we checked that, for example, FeSi and MnSi in the sixfold coordinated rock-salt structure show *no* band gap in their DOS, even though the B20 structure is a distorted form of the rock-salt structure.) We inspected this in more detail for the representative case of FeSi. As in all studied TM-Si compounds (cf. Fig. 2), the TM $3d$ states dominate the DOS around the Fermi energy. From Fig. 3 one can see that the ubiquitous band gap actually separates two groups of bands which have predominantly either a Fe $3d_{x^2-y^2} + 3d_{xy}$ character (top of the valence band, VB) or a Fe $3d_{xz} + 3d_{yz}$ character

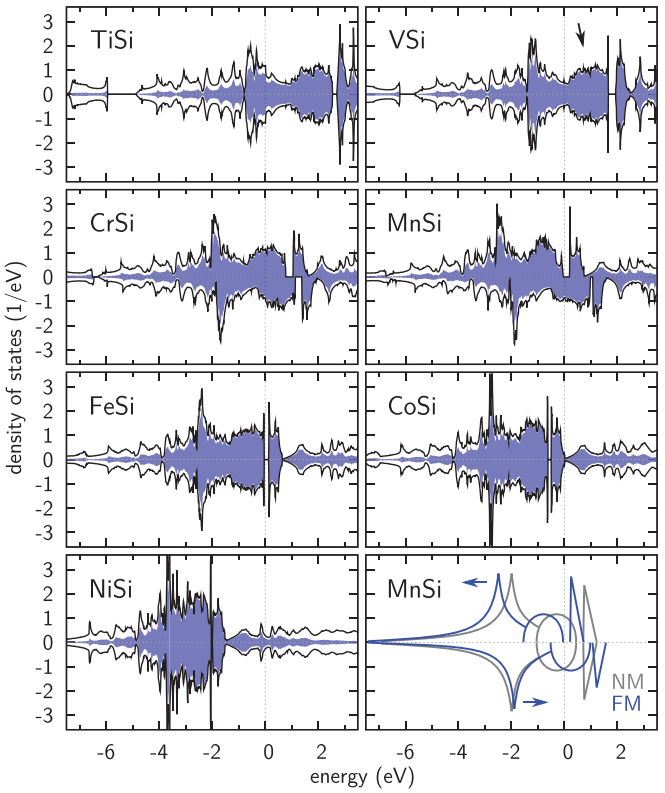

FIG. 2. (Color online) Spin-resolved DOS for different TM monosilicides in B20 structure. The black lines indicate the total DOS per f.u., and the blue shaded areas correspond to the projection onto the TM $3d$ orbitals. The Fermi energy is chosen as reference energy. The black arrow in the VSi panel marks the "hill" referred to in the text. The bottom-right panel schematically indicates the origin of magnetism for MnSi.

(bottom of the conduction band, CB), where the orientation of the $3d_{z^2}$ orbital has been chosen parallel to the [111] direction of the cubic unit cell. The two opposing band groups can also be identified clearly in band structure plots with superimposed band character [Fig. 3(c)]. How the difference between these two groups manifests itself in the crystal environment can be seen from sections through the integrated local density of states (ILDOS), which is defined as

$$I(\mathbf{r}) = \left| \int_0^E d\varepsilon \sum_{n\mathbf{k}} |\psi_{n\mathbf{k}}(\mathbf{r})|^2 \, \delta(\varepsilon - \varepsilon_{n\mathbf{k}} + E_\mathrm{F}) \right|,$$

with Kohn-Sham states $\psi_{n\mathbf{k}}$, energy eigenvalues $\varepsilon_{n\mathbf{k}}$, and the Fermi energy E_F. We have used $E = +1$ eV ($E = -1$ eV), which covers the lowest conduction band (highest valence band) states [Fig. 3(b)]. The (111) lattice planes have been chosen such as to contain three Fe atoms forming a triangle (that is, a dense Fe layer). These TM-TM triangles are characteristic for the B20 structure since they build up the trillium lattice (cf. Ref. 51). In addition to the expected localization around the Fe centers the ILDOS shows that the highest VB orbitals point with one lobe into the centers of Fe-Fe triangles, whereas the lobes of the lowest CB states point more or less along the triangle edges. This is in line with previous findings by Andersen *et al.*[52] It is reasonable to

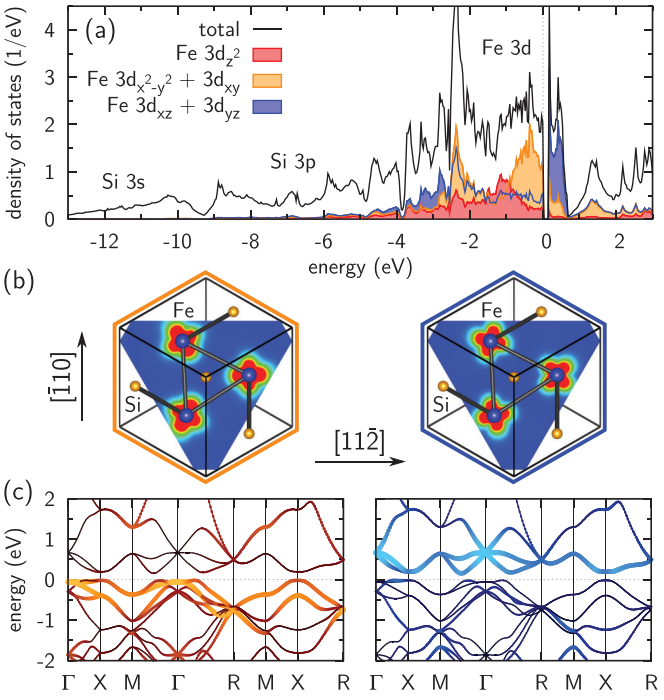

FIG. 3. (Color online) Electronic structure of bulk FeSi in B20 structure. (a) DOS plot in which the black line indicates the total DOS per f.u. and the red, orange, and blue shaded areas correspond to projections onto the Fe $3d_{z^2}$, $3d_{x^2-y^2} + 3d_{xy}$, and $3d_{xz} + 3d_{yz}$ orbitals. The $3d_{z^2}$ orbital lies parallel to the [111] direction of the cubic unit cell. The Fermi energy is chosen as reference energy. (b) ILDOS sections along a characteristic (111) lattice plane in the cubic unit cell showing the spatial orientation of the topmost VB (left) and lowest CB (right) states in the crystal (cf. Fig. 1). As the ILDOS value increases, the plane color shifts from blue to red. (c) Band structure plots around the Fermi energy in which the band character is indicated by color and size. Thick bands with bright orange (bright blue) colors correspond to a strong $3d_{x^2-y^2} + 3d_{xy}$ ($3d_{xz} + 3d_{yz}$) band character.

assume that this band and orbital structure carries over to all other B20 materials in the scope of this paper.

All considered materials in B20 structure are found to be metallic, except FeSi, which is a semiconductor at low temperatures. The DOS of CoSi exhibits only small values at the Fermi energy; therefore, CoSi is a metal with low conductivity. NiSi is also metallic in its ground state crystal structure B31. These results agree nicely with experimental observations.[6] For TiSi in B27 structure, we also find a metallic behavior.

We find a preference for the FM ground state for CrSi and MnSi. In this context, the origin of magnetism can be understood in a simple Stoner picture. By inspecting the DOS in Fig. 2 we can see that the "hill" (marked by a black arrow) between the position of the Fermi energy for VSi and the band gap (in which the Fermi energy for FeSi lies) can be filled with three electrons. For VSi, the hill is empty and the Fermi energy lies in a local minimum; an exchange splitting would not lead to a lowered total energy here. For CrSi and MnSi, the hill is partially filled with one or two electrons. In this situation, a NM solution is expected to be metastable. Indeed, in the case of CrSi, the exchange splitting shifts the bands such that the Fermi energy lies roughly in the center of the hill for the majority spins and slightly above the local minimum for the minority

spins. For MnSi, the Fermi energy lies at 1/3 filling of the hill for the minority spins and in the band gap for the majority spins. The NM-FM transition for MnSi is schematically displayed in the bottom-right panel in Fig. 2, where the gray (blue) lines depict the initial NM (final FM) situation. Finally, for FeSi, the hill is filled completely and the Fermi energy lies in the band gap for both spin channels. For CoSi and NiSi, the Fermi energy lies in stable local minima again. Therefore, these materials are NM, in agreement with the literature.[6]

For CrSi, the energy splitting between the NM and the FM configuration at their respective equilibrium lattice constants is very small (1.6 meV per f.u.). This indicates a high fluctuability of the localized magnetic moments (0.45 μ_B per Cr in the FM phase) and agrees with the general view of CrSi as being a weak Pauli paramagnet,[6,41] especially at room temperature.

The FM phase in MnSi is found to be far more stable with a NM-FM energy splitting of 61 meV per f.u. It is predicted to be half metallic: In the majority spin channel, the Fermi energy lies in the small indirect band gap (0.23 meV calculated width in DOS), close to the "valence band maximum," while the minority spin channel behaves metallic. Consequently, the magnetic moment takes an integer value (1 μ_B per f.u.). This remains the case for lattice constants ranging from approximately 4.49 to 4.61 Å. For larger lattice constants we find a sudden transition to a higher spin state, in which the total magnetic moment approaches 2 μ_B per f.u.

FeSi is NM in our zero-temperature calculations, in agreement with previous theoretical work.[12,25,50,53] It shows signs of ferromagnetism for increased lattice constants in our calculations, but this magnetic configuration remains about 30–35 meV per f.u. higher in energy than the NM solution and thus is only metastable. It is difficult to extract the exact DFT energy of the FM state because of a NM-FM jump occurring very close to the equilibrium position [cf. Ref. 25, Fig. 1(d)]. For the same reason we can only give an upper bound for the magnetic moment of 0.92 μ_B per f.u. for the FM state. The band gap has a width of 0.16 meV according to our GGA calculations, which agrees roughly with previously reported LDA values,[12,50,53] but is too large when compared to values derived from recent experiments.[42,43,48,49] Note that usually band gaps are *underestimated* by conventional DFT. Dynamical correlations accounted for in LDA + DMFT calculations reduce the width of the band gap by approximately a factor of 2.[12]

Since magnetic properties are a delicate issue and can significantly depend on the pseudopotential, we checked the agreement of our CrSi, MnSi and FeSi USPP results with LAPW calculations. For CrSi we find a total magnetic moment of 0.44 μ_B per f.u., which is in line with our pseudopotential result (cf. Table I). As expected, due to the presence of the band gap, the integer magnetic moments for MnSi and FeSi are reproduced as well. Especially, the half metallic character of MnSi is no artifact of the pseudopotential approach. Furthermore, the magnetic transition to a higher spin state in expanded MnSi has been verified with LAPW.

IV. Si(111)-STRAINED BULK PROPERTIES OF DIFFERENT TRANSITION METAL MONOSILICIDES

For epitaxial films of about 20 nm thickness, a value typically used in experiments,[3,5,54] surface, interface, and confinement effects are minor and the film properties are dominated by a strained-bulk behavior. It is well established (see, for example, Refs. 3,5,9,10, and 54–60) that an epitaxial B20 TM monosilicide film on Si(111) will grow in [111] direction since its hexagonal unit cell parameter a_{hex} fits closely to the Si(111)-($\sqrt{3} \times \sqrt{3}$) surface lattice constant if Si[01$\bar{1}$] ∥ TM-Si[11$\bar{2}$]. It will be distorted in the lateral plane, and the small misfit strain is compensated by an accommodation of the unit cell height c_{hex} and the atomic coordinates.

Our calculated DFT-PBE Si(111)-(1 × 1) lattice constant is $5.468\,\text{Å}/\sqrt{2} = 3.866\,\text{Å}$, deviating by +0.7% from the experimental value of 3.840 Å. This translates to a Si(111)-($\sqrt{3} \times \sqrt{3}$) lattice constant of $a_{\text{Si(111)}}^{\sqrt{3}\times\sqrt{3}} = 6.697$ Å (6.650 Å experimentally). The simple cubic unit cells of the TM monosilicides can be transformed to a hexagonal cell with the [111] direction pointing along the z axis (cf. Fig. 1): $a_{hex} = \sqrt{2}\,a_{cub}$, $c_{hex} = \sqrt{3}\,a_{cub}$. From Table I it follows that $a_{hex} = 6.491$ (6.546), 6.387 (6.446), 6.286 (6.354) Å for CrSi, MnSi, and FeSi, respectively. (Experimental values are given in parentheses.) Thus, DFT-PBE overestimates the Si lattice constant, while giving slightly underestimated TM-Si lattice constants. As a consequence, the lattice mismatch between the Si(111) substrate and a TM-Si film will be overestimated and the in-plane tensile strain in the thin film will be higher in our calculations than in reality. The calculated (experimental) lattice mismatches are 3.2% (1.6%), 4.9% (3.2%), and 6.5% (4.7%) for CrSi, MnSi, and FeSi, respectively. To assess the significance of these deviations (for example, in how far the phenomena related to strain effects will also be overestimated), we studied the influence of biaxial strain over a large lattice constant interval (see below).

In the hexagonal unit cell (cf. Fig. 1), the z axis coincides with the [111] direction of the simple cubic unit cell. Along this [111] direction, the structure is repeated after 12 individual layers. Four layers can be grouped into one quad-layer (QL), which then consists of a Si-dense, TM-sparse, Si-sparse, and TM-dense layer.[9,10] In unstrained bulk material, atoms in sparse and dense layers are all equivalent.

The calculations for Fig. 4 were carried out using such a hexagonal unit cell. For each pair of cell parameters (a,c) a full relaxation of the internal atomic coordinates was performed. Figure 4(a) shows total energy curves for different c at fixed $a = a_{\text{Si(111)}}^{\sqrt{3}\times\sqrt{3}}$ for CrSi, MnSi, and FeSi. In order to get an impression of the spin stiffness, we studied different spin configurations in our hexagonal unit cell. We assumed that the TM magnetic moments in one and the same layer are equal, while those of different layers were allowed to have a different magnitude and, possibly, an antiparallel orientation. This seems reasonable since the application of strain lifts the symmetry equivalence between sparse and dense layers for TM and Si atoms. In addition to the NM case and the FM ordering, we looked into a partially compensating "ferrimagnetic" (FIM) pattern that emerges from a cosinelike starting configuration of the TM magnetic moments:

$$m_{\text{TM}}^{\ell} = m_{\text{TM}}^{0} \cos(q\ell), \tag{1}$$

where ℓ denotes the TM layer index, counting in [111] direction and starting with zero for a TM-sparse layer (cf. Fig. 1). For the moment we restrict ourselves to $q = \pi/3$,

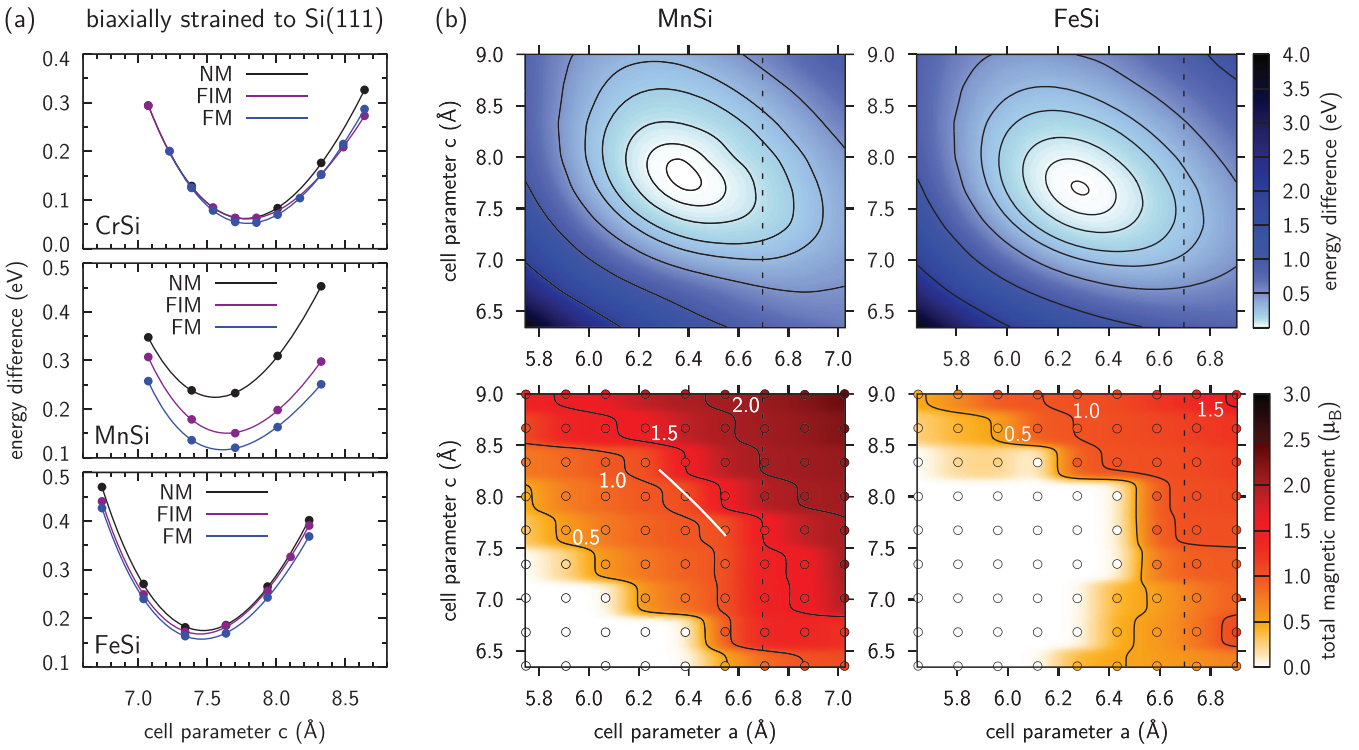

FIG. 4. (Color online) (a) Graphs showing the total energy per f.u. of different magnetic configurations (NM, FIM with $q = \pi/3$, FM) in CrSi, MnSi, and FeSi under biaxial strain as a function of the hexagonal unit cell height c. The lateral lattice constant is $a = a_{\mathrm{Si(111)}}^{\sqrt{3}\times\sqrt{3}}$. The energy values are differences with respect to the corresponding strain-free bulk structure. (b) Energetic and magnetic maps of MnSi and FeSi as functions of the hexagonal cell parameters a and c. Color encoded, the energy difference with respect to the corresponding strain-free bulk structure (upper row) and the total magnetic moment (lower row) per f.u. is shown. The black circles indicate the positions of calculated values and are filled with the corresponding color; the remaining area is interpolated. The vertical dashed lines mark $a = a_{\mathrm{Si(111)}}^{\sqrt{3}\times\sqrt{3}}$. The white curve in the MnSi magnetic moment map indicates the parameter range for the rhombohedral unit cell used in Ref. 19 according to Eqs. (3), where the magnetic moment was found to be constant (1 μ_{B} per f.u.).

for which the modulation fits into a single hexagonal unit cell. Note that this initial pattern leads to a net total magnetic moment in practice, in contrast to a perfect antiferromagnetic (AFM) ordering, even though the mean of the cosine vanishes. The reason is that the cosine is superimposed by the sparse-dense layer structure, and in addition to the different TM density, TM-sparse and TM-dense layers can bear different local magnetic moments, especially if biaxial strain is applied.

As one can see from Fig. 4(a), the FIM configuration ($q = \pi/3$) is always higher in energy than the FM configuration. An exception is CrSi at high vertical expansion, where the FIM ordering is lowest in energy. However, at the equilibrium height of the cell (c), the FM ordering is always lowest, even for CrSi. Especially, this means that FeSi becomes ferromagnetic under epitaxial strain. The distances between NM, FIM, and FM curves and equilibrium energies are largest for MnSi and only small for CrSi ($\approx$10 meV/f.u.) and FeSi (NM-FM 17.7 meV/f.u., FIM-FM 10.5 meV/f.u.). We speculate on this basis that the Curie temperature will be very low for the latter two. The equilibrium heights of the hexagonal cells are 7.79, 7.61, and 7.46 Å for CrSi, MnSi, and FeSi in their FM phase, respectively. From this follows the height of a single QL to be about 2.4–2.6 Å in bulk, depending on the material. Thus, a thin film of 20 nm thickness consists of approximately 310–330 layers of TM-Si.

Since MnSi and FeSi appeared most interesting to us and experimental data of samples with a high degree of structural quality exists in the literature, we will focus on them in the following. In Fig. 4(b) results for a wide range of planar lattice constants a and cell heights c are shown: Color-encoded maps display the total energy relative to the ground state without strain and the total magnetic moment. For each data point we compared a FM calculation to a NM calculation. We found that the FM calculations sometimes have the tendency to converge to metastable solutions with finite magnetic moment, while the solution of the corresponding NM calculation is actually lower in energy. This has been taken into account by assigning a magnetic moment of zero to points with only metastable magnetic solutions. A further, similar complication was that for some points the calculated magnetic moments did not fit seamlessly into their neighborhood. In this case, we performed additional calculations with reasonably constrained total moments, followed by calculations without constraints which started from the previously obtained potential. Usually the new energy turned out to be smaller and the original result was replaced. However, this procedure did not work for all points; for example, the area around the small feature on the lower right side in the FeSi magnetic moment map was stable against all our checks. The FIM configuration was examined at some points, especially at the corners of the map and along

TABLE III. Volume expansion $V^{\mathrm{PBE}}_{\mathrm{Si(111)}}$ and total magnetic moment $M^{\mathrm{PBE}}_{\mathrm{Si(111)}}$ of different TM-Si bulk structures laterally strained to the Si(111) surface lattice constant $a^{\sqrt{3}\times\sqrt{3}}_{\mathrm{Si(111)}}$. The strain-free volume $V^{\mathrm{PBE}}_{\mathrm{GS}}$ is determined from Table I. In parentheses, localized magnetic moments at the TM sparse/dense atoms are listed. All values are given per f.u.

	$V^{\mathrm{PBE}}_{\mathrm{GS}}$ (Å^3)	$V^{\mathrm{PBE}}_{\mathrm{Si(111)}}$ (Å^3)	$M^{\mathrm{PBE}}_{\mathrm{Si(111)}}$ (μ_{B})
TiSi	30.73	31.51 (+2.5%)	0.00
VSi	26.54	26.54 (+0.0%)	0.00
CrSi	24.18	25.22 (+4.3%)	0.63 (0.64/0.72)
MnSi	23.03	24.63 (+7.0%)	1.50 (1.22/1.85)
FeSi	21.96	24.13 (+9.9%)	0.99 (0.57/1.30)
CoSi	21.73	23.84 (+9.7%)	0.00
NiSi	23.01	24.01 (+4.3%)	0.00

$a^{\sqrt{3}\times\sqrt{3}}_{\mathrm{Si(111)}}$, and nowhere found to be lowest in energy. In both energy maps, the minimum is consistent with the ground state cell parameters a_{hex} and c_{hex} given above. Obviously there are no other local minima for $c(a)$ than the ground state (apart from metastable magnetic configurations). The magnetic maps in Fig. 4(b) show that for compressive strain the magnetic moment tends to decrease, whereas for tensile strain it increases, obviously even beyond our Si(111) value. The NM region is much larger for FeSi than for MnSi. For FeSi, the area with finite magnetic moment is sickle shaped. However, in the vicinity of the NM region, the energetic stability of these moments is very low. The maps demonstrate that our results are stable against small variations of the surface lattice constant; especially, using the experimental value for Si(111) would not lead to significant changes. Thus, the slightly overestimated lattice mismatch is irrelevant.

As already mentioned, a FM ground state is predicted for biaxially strained FeSi, with a total magnetic moment of 0.99 μ_{B} per f.u. Since FeSi is semiconducting in the unstrained bulk case, a transition to a metallic, magnetic phase has to occur for a critical value of the biaxial tensile strain. Furthermore, we find a volume expansion of 9.9% (Table III). Recently, the volume expansion in epitaxial FeSi thin films of 20 nm thickness on Si(111) was experimentally measured by Porter *et al.*[5] Within their error bars, they found a volume difference between polycrystalline films, which they concluded to be a strain-free reference, and epitaxial films of approximately 10%. A similar effect was found for $Fe_{0.5}Co_{0.5}Si$, together with an increased Curie temperature (33%) and a higher saturation magnetization (Fig. 4 in Ref. 5). Their FeSi result agrees even quantitatively with our calculations. Although we did not study $Fe_{0.5}Co_{0.5}Si$ explicitly, we can deduce from our results on FeSi and CoSi that the intermediate alloy will behave similarly with respect to the volume expansion. The electronic properties should be somewhere in between: CoSi is already weakly metallic without tensile strain and provides additional electrons to the distorted, metallic FeSi, so we expect strained $Fe_{0.5}Co_{0.5}Si$ to be a metal as well. From their transport measurements on FeSi, where strained and unstrained material are being compared, one could deduce that the band gap prevails, although becoming narrower. However, the overall resistivity they observe is quite small. Older ultraviolet photoelectron spectroscopy studies of FeSi thin films on Si(111) were unable to resolve a gap and found a metallic state.[61] Our DOS for epitaxial FeSi (Fig. 5) indicates a metallic behavior with a high degree of spin polarization at the Fermi energy. For $Fe_{0.5}Co_{0.5}Si$/Si(111), a metallic conductivity has been observed in experiment,[5] which proves the correctness of our aforementioned expectation.

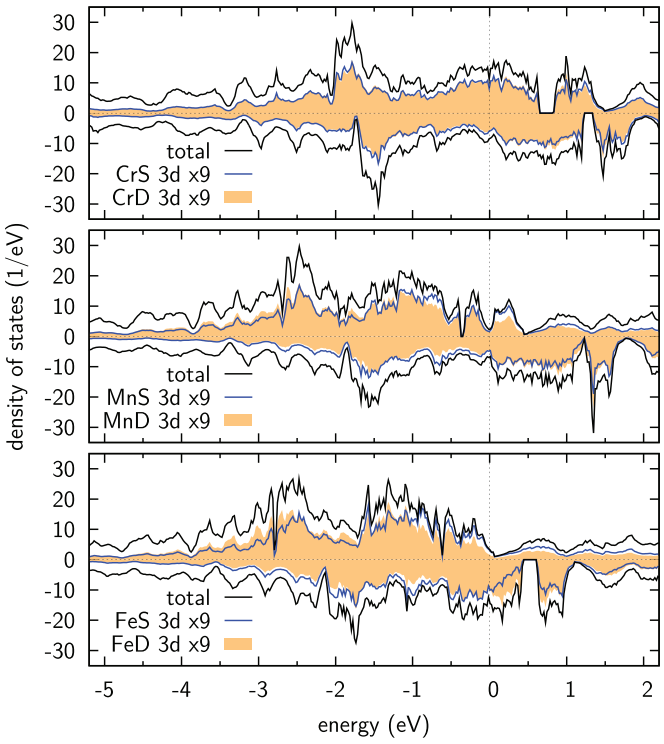

FIG. 5. (Color online) Spin-resolved total DOS (black lines) per hexagonal unit cell for bulk CrSi, MnSi, and FeSi (from top to bottom) under biaxial strain ($a = a^{\sqrt{3}\times\sqrt{3}}_{\mathrm{Si(111)}}$) and projections onto sparse (S, orange shaded areas) and dense (D, blue lines) TM atoms. The respective Fermi energies have been chosen as reference.

For MnSi, a volume expansion by 7% as well as an increase of the magnetic moment by 50% can be seen (cf. Fig. 4 and Table III). Interestingly, we find in addition a significant stabilization of the FM alignment: The energy splitting $E_{\mathrm{FIM}} - E_{\mathrm{FM}}$ between the FIM magnetic ordering ($q = \pi/3$) and the FM ordering is 18.5 meV in the case of bulklike, unstrained MnSi. Due to biaxial strain this value increases by 88% to 34.7 meV. We also looked at a third configuration: A perfectly compensating AFM ordering with vanishing total magnetic moment can be produced by flipping the moments with QL periodicity (two Mn layers up, two Mn layers down, etc.):

$$m^{\ell}_{\mathrm{Mn}} = m^{0}_{\mathrm{Mn}}\,\{2\Theta\,[\cos(q\,\{\ell - 1/2\})] - 1\}\,, \quad q = \pi/2. \qquad (2)$$

In this case, however, a hexagonal cell with 24 layers is necessary. The different magnetic configurations are visualized in Fig. 6. The energy splitting $E_{\mathrm{AFM}} - E_{\mathrm{FM}}$ between this QL AFM texture and the FM ground state is 33.2 meV per f.u., so it is more unfavorable than the FIM configuration. Under strain this value increases by 85% to 61.5 meV. Following the thought that roughly $T_{\mathrm{C}} \sim |E_{\mathrm{FM}} - E_{\mathrm{AFM}}| \sim |E_{\mathrm{FM}} - E_{\mathrm{FIM}}|$, this means that the Curie temperature should show a significant increase. Indeed, Karhu *et al.* observed such a trend in their

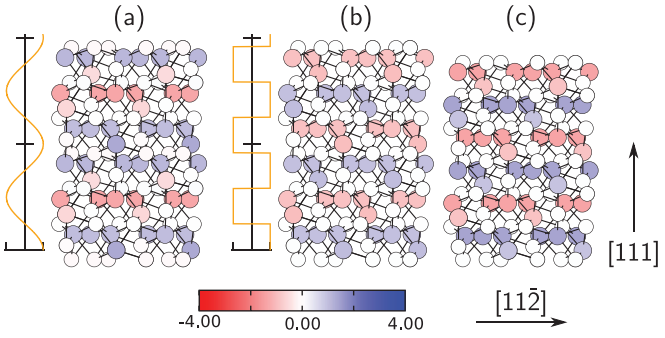

FIG. 6. (Color) Different metastable antiparallel magnetic configurations in MnSi. Small, almost white (big, colorful) spheres depict Si (Mn) atoms. The colors represent the local magnetic moment (in μ_B) at the different atoms. (a) Cosine-shaped pattern according to Eq. (1) for $q = \pi/3$ in strain-free MnSi. (b) Perfectly compensating AFM ordering with QL steps according to Eq. (2) in strain-free MnSi. (c) As (b), but for MnSi epitaxially strained to fit the Si(111) surface. Note the different magnetic moment magnitude for sparse and dense atoms, which reflects the strain-induced symmetry break.

MnSi/Si(111) films. While they found only a small increase of the saturation magnetization [maximally 8% according to Fig. 8(b) in Ref. 3], they reported a value of $T_C \approx 43$ K for films of 10 nm thickness and above.[3,4] This corresponds to an increase of about 46%. Thus, our calculations predict the correct trend, while one cannot expect quantitative agreement, since the inclusion of nonlocal electronic correlations and a calculation of T_C is beyond the scope of our work. Moreover, this result indicates that MnSi cannot be fully described as a simple Heisenberg ferromagnet with localized moments: Given that the exchange constants in a Heisenberg model are typically decreasing functions of the interatomic distance, an increased volume and increased average Mn-Mn distances should lead to a weaker magnetic coupling. This is contrary to our calculations and to the experimental findings, and points to the importance of itinerant exchange for the magnetic ordering in MnSi.

As expected from the noninteger total magnetic moment, the Fermi energy has moved out of the half metallic gap in which it is located for strain-free MnSi (cf. Fig. 5). Instead, it shifts to the next stable DOS valley in the majority channel, transferring 1/4 electron per f.u. from the minority channel to the majority channel. The feature above the Fermi energy in the majority channel, which can take 1/2 electron per f.u. and spin channel according to the FeSi and CoSi panels in Fig. 2, is split and half filled. For strained FeSi, it is filled completely, and the Fermi energy sits at the same position in the majority channel as for strain-free CoSi. The DOS for strained CrSi shows only small differences compared to the strain-free case. Remnants of the band gap can still be seen for all three compounds in both spin channels.

We looked for a similar strain effect also in bulk TiSi, VSi, CoSi, and NiSi, but found no signs of FM order, just like in the case of unstrained bulk. Hence, the respective values in Table III are from NM calculations.

Again we checked our USPP results with all-electron LAPW calculations. Although we did not aim at high-quality LAPW results, the method produced densities of states that were very similar to those in Fig. 5. We found total magnetic moments of 1.46 μ_B for MnSi and 1.00 μ_B for FeSi. Comparison with our USPP results (Table III) shows excellent agreement. Thus, we can exclude that our observations are just pseudopotential artifacts: The strain-increased (strain-induced) magnetic moment is also seen in LAPW for MnSi (FeSi).

The strain-induced symmetry break can be observed by looking at the localized magnetic moments, e.g., of the TM atoms, as listed in Table III or visualized for MnSi in Fig. 6(c). For Si(111)-strained CrSi, MnSi, and FeSi, the localized moments at the sparse and dense atoms are not equal anymore and larger than those in the unstrained material. Especially, the magnetic moment at the dense atoms is larger than that at the sparse atoms. At the Si atoms, an antiparallel moment of approximately −0.07, −0.19, and −0.12 μ_B is induced for CrSi, MnSi, and FeSi, respectively, which reduces the total magnetic moment. The induced antiparallel moment already exists without strain and is a phenomenon that can be observed in other TM compounds as well, for example in Heusler alloys.[62] The inequivalence can also be seen in the structural properties, e.g., in the distances between the TM atoms, which, neglecting the Si atoms, form a trillium lattice[51] of sixfold coordination. In the unstrained case, all TM-TM distances are the same: 2.77 Å for MnSi and 2.73 Å for FeSi. For MnSi (FeSi) subject to Si(111) epitaxial strain we find dense-dense intralayer 3.01 Å (2.92 Å); dense-dense interlayer 2.68 Å (2.66 Å); sparse-dense, crossing Si-sparse layer 2.83 Å (2.84 Å); and sparse-dense, crossing Si-dense layer 2.81 Å (2.85 Å). The behavior is very similar for MnSi and FeSi: All TM-TM distances increase, except the dense-dense interlayer distance. As a consequence, four different coupling constants are necessary if one wants to model this system by a nearest-neighbor Heisenberg Hamiltonian.

Karhu *et al.* studied the effect of biaxial strain on the uniaxial anisotropy using DFT (full-potential local-orbital method) and a rhombohedral unit cell with different values for the rhombohedral angle Ξ around $\pi/2$.[19] They found no deviations of the total magnetic moment from the usual bulk value of 1 μ_B per f.u. Using the equations

$$\begin{aligned} a_{\mathrm{hex}}(\Xi) &= a_{\mathrm{cub}}^{\mathrm{MnSi}} \sin(\Xi) \sqrt{\frac{2\sqrt{3}}{\sqrt{[1+2\cos(\Xi)]^2 + 2\sin(\Xi)^2}}}, \\ c_{\mathrm{hex}}(\Xi) &= a_{\mathrm{cub}}^{\mathrm{MnSi}} \sqrt{[1+2\cos(\Xi)]^2 + 2\sin(\Xi)^2}, \end{aligned} \tag{3}$$

with their MnSi lattice constant $a_{\mathrm{cub}}^{\mathrm{MnSi}} = 4.556$ Å we can connect their results to ours. Their parameter range is displayed as a white line in the magnetic moment map of MnSi in Fig. 4(b). Indeed, we find complete agreement between both calculations: Around the white line, our magnetic moment is constant. The reason is most certainly the half metallic gap predicted by DFT, in which the Fermi energy can move for some time under strain before the total magnetic moment starts to change (Fig. 2).

We used such a distorted rhombohedral unit cell, adapted to our optimized cell parameters given above, to calculate exemplarily the phonon band structure of strained MnSi employing the density functional perturbation theory approach.[63] No

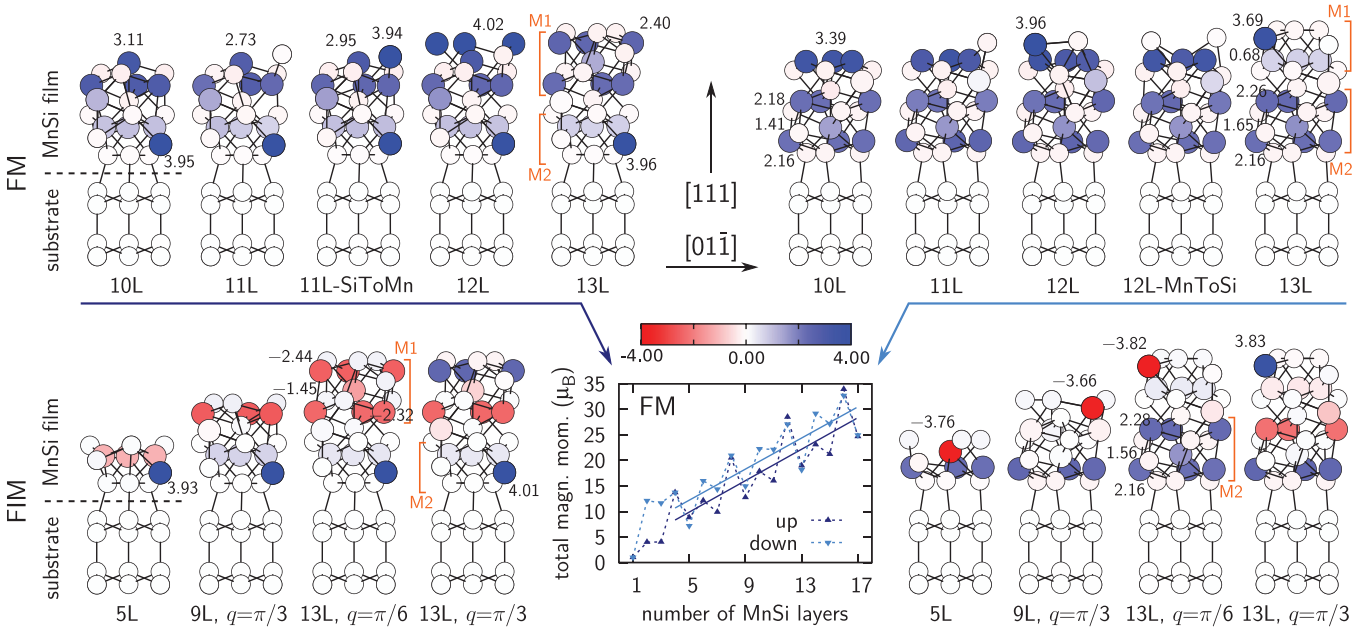

FIG. 7. (Color) Atomic structures and magnetic configurations of MnSi thin films of selected thickness together with two bilayers of the Si substrate. The left (right) structures reflect the up (down) MnSi stacking. The upper (lower) row shows configurations of parallel (antiparallel) Mn spin alignments. Small, almost white (big) spheres depict Si (Mn) atoms. The color encoding shows the local magnetic moments (μ_B). For convenience, the value is explicitly written out for selected Mn atoms. Note also that single atoms represent complete layers of similar atoms. M1 and M2 denote two spin motifs that arise frequently in the magnetic configurations. The inset shows the dependence of the total magnetic moment on the number of film layers n for FM alignment and two linear fits for up and down stacking.

imaginary frequencies have been found, which corroborates the dynamical stability of the strained B20 bulk structures.

V. MnSi THIN FILMS ON Si(111)

Since MnSi showed the most significant response to epitaxial strain, we explicitly studied thin films of MnSi in B20 structure on Si(111), varying the film thickness and the magnetic configuration.

MnSi thin films can grow in two possible stacking sequences on Si(111) which we named "up" and "down" (cf. Fig. 1 in Ref. 10). The growth takes place with a thickness unit of single QLs,[58,60] which can be explained by calculations of surface and film formation energies.[10] Furthermore, since the TM monosilicides in B20 structure are noncentrosymmetric, two possible structural chiralities exist. Since the crystalline chirality determines the magnetic helicity, the two chiralities can be distinguished using x-ray and polarized neutron small-angle diffraction[64,65] or dark-field transmission electron microscopy imaging.[3,4] However, since "left- and right-handed" structures can be interchanged by a mirror operation (involving a plane containing the [111] and [11$\bar{2}$] axes), which leaves the Si(111) substrate invariant, both chiralities are energetically degenerate, and we can restrict ourselves to up and down structures with one chosen handedness. Actually, coexisting domains of left- and right-handed chirality have been found in MnSi films.[3]

In the previous section we have argued that the behavior of thicker films can be described by strained bulk material. However, the thinner the films, the more important are surface, interface, and confinement effects. Since the repetition period of the layer structure is quite large (12 layers, see above), these effects will not be restricted to ultrathin films, but may become noticeable even in films of a few nanometers of thickness.

We studied film structures with up to 17 layers of MnSi. The same geometry as in our previous study of MnSi/Si(111) thin films has been used.[10] The bonding of the films to the substrate is made between a single-dangling-bond termination of Si(111) and a Si-dense termination of MnSi(111) for both up and down stacking of MnSi. In Fig. 7, upper row, one can see the relaxed atomic structure of the interface. A significant difference exists between the up and the down stacking, where the length of the Si-Si bond connecting the substrate and the thin film is 2.36 and 2.40 Å, respectively. On the other hand, the dependence on the film thickness is negligible (±0.01 Å). For comparison, the Si-Si bond length in our bulk Si is ≈2.37 Å. Additionally, two nonstoichiometric structures are shown: An 11-layer structure in up stacking, where the topmost Si has been replaced by Mn, and a 12-layer structure in down stacking, where the topmost Mn has been replaced by Si. The former is interesting from the viewpoint of our previous work, where it appeared as possible "2-Mn-dense" surface termination of films grown by reactive epitaxy.[10]

The single-dangling-bond–Si-dense interface is an assumption we made, based on the fact that the *surface* energy of Si-dense terminated films is minimal under Si-rich conditions,[10] which will certainly be present at the interface. In addition, we calculated the associated interface energy γ from a fully optimized, periodic Si-MnSi-Si sandwich structure using an *ab initio* thermodynamic approach:[66]

$$\gamma = \frac{1}{2A}\{E_{\text{tot}} - (N_{\text{Si}} - N_{\text{Mn}})\mu_{\text{Si}} - N_{\text{Mn}}E_{\text{MnSi}}\}.$$

Here E_{tot} and E_{MnSi} are the DFT total energies of the sandwich structure and laterally distorted MnSi bulk, respectively; the N_i are the numbers of atoms in the structure, A is the interface area, and $\mu_{\mathrm{Si}} = E_{\mathrm{Si}}$ is the chemical potential of Si, which takes the energy of Si bulk to model Si-rich growth conditions. The result is $\gamma = 75$ meV/Å^2, a value that is significantly smaller than the surface energy of the relaxed bare Si(111)-single-dangling-bond surface ($\gamma \approx 95$ meV/Å^2) or the mean of the MnSi(111)-Si-dense surface energies ($\gamma \approx 102$ meV/Å^2) under the same growth conditions, which we also determined. Note that due to the missing inversion symmetry there are two inequivalent Si-dense terminated interfaces in the sandwich structure, and γ is an average over both of them. The individual contributions are hard to isolate, a problem similar to the case of GaAs(111).[67]

The dependence of the local magnetic moments on the film thickness can be seen in Fig. 7. Obviously the Mn moments at both the interface and the surface deviate strongly from their values in strained bulk material (cf. Table III). This is especially striking for the Mn-sparse atom close to the interface in up stacking. The weak, induced antiparallel Si moments in the MnSi films can be seen, too. The values of the interface Mn magnetic moments converge quickly with increasing interface-surface spacing. Any Si surface termination reduces the magnetic moment of the subsurface Mn layer, especially a Si-dense termination. Comparison with thicker films (not shown) indicates that the shown surface behavior of the magnetic moments is repeated periodically.

The total magnetic moment of our film structures increases with each new layer of Mn and decreases again slightly as the successive Si layer is deposited (cf. Fig. 7, inset). We fitted the total magnetic moments as function of the number of MnSi layers n to linear functions $f(n) = a\,n + b$ separately for up and down stacking. The results are slopes $a = 1.54\ \mu_{\mathrm{B}}$ ($1.52\ \mu_{\mathrm{B}}$) and offsets $b = 2.15\ \mu_{\mathrm{B}}$ ($4.58\ \mu_{\mathrm{B}}$) for up (down) stacking. For both stacking sequences, the slope is already very close to the value obtained for bulk material under strain (cf. Table III). The different offsets are due to the different magnetic structure of up and down stacked films at the interface (cf. Fig. 7).

Similar to our procedure in the previous section, we studied also different antiparallel (FIM) spin configurations within our collinear approximation in film structures with 5, 9, and 13 layers of MnSi in up and down stacking, all being terminated by a Si-dense layer (Fig. 7, lower row). Since the 5-layer ultrathin films contain just two Mn layers, there are only two magnetic configurations: parallel or antiparallel. For the 9- and 13-layer structures, we simulated cosine- and QL-shaped magnetic orderings starting from initial moments that follow Eqs. (1) with $q = \pi/3$ and (2). In the 13-layer structures we used $q = \pi/6$ in addition, which results in a single smooth flip of the magnetic moment direction. In all cases, the QL AFM pattern was unstable and converged to the cosine pattern with $q = \pi/3$. This is in contrast to the bulk case, where the perfectly compensating QL AFM configuration was at least metastable, as discussed in the previous section.

The energy differences of these magnetic configurations with respect to a FM alignment in structures of similar thickness can be seen in Table IV. The ultrathin 5-layer structures, especially the one in up stacking, prefer a parallel spin alignment. Here quantum confinement effects in the film are very strong. For thicker films, the situation is surprisingly different: The FIM configurations are lower in energy than the FM ones, independent of the stacking. Both up and down 9-layer structures benefit most from the sign flip in the magnetic pattern; the energy difference is smaller for the 13-layer structures. Furthermore, in the 13-layer structures, a double flip with $q = \pi/3$ is less favorable than a single flip with $q = \pi/6$. We assume that for even thicker films, the energy benefit of a partially compensating magnetic order will decrease further, finally turning into a preference of unidirectional alignment.

TABLE IV. Energy differences (meV) per hexagonal $\sqrt{3} \times \sqrt{3}$ supercell of different FIM configurations (cf. Fig. 7, bottom row) with respect to FM configurations in MnSi thin films on Si(111). Positive values indicate a more stable FM configuration. The "bulk" values are expectations extrapolated from the strained-bulk results of the previous section.

Stacking	5L	9L, $q = \pi/3$	13L, $q = \pi/6$	13L, $q = \pi/3$
Up	+215	−50	−45	−32
Down	+20	−136	−126	−76
Bulk	+139	+278	+416	

It is interesting to compare these results to expected values that can be extrapolated from the strained-bulk results of the previous section by multiplication with the number of MnSi formula units contained in the film structures (Table IV). For 5 layers in up stacking, the FM configuration is more stable than expected, while it is much weaker than expected for the down stacking. For 9 layers, the energy spacing FIM-FM is not only negative, but also smaller in absolute value than the expectation. This is even more pronounced for 13 layers.

We confirmed the reliability and reproducibility of our results by performing a structural relaxation with FM spin orientation starting from FIM $q = \pi/6$ final coordinates for a 13-layer structure. The result agreed with our original FM calculation, which shows that indeed the magnetic structure is responsible for the energy differences.

In the different parallel and antiparallel magnetic configurations, certain recurring spin motifs can be identified, especially in the 13-layer structures (cf. Fig. 7). Of course, the motifs can appear in a spatial- and spin-inverted form. The magnetic pattern of the 13-layers down structure resembles strongly an upside-down version of its counterpart in up structure, regardless of interface and surface. Even the total magnetic moments are very similar. A major difference for both up and down stacked 13-layer films between $q = \pi/6$ and $q = \pi/3$ is the parallel and antiparallel spin orientation in the upper layers (motif M1). Thus, the FM order in motif M1 is presumably responsible for the lower energy of the $q = \pi/6$ configuration.

Our conclusions from aforementioned observations are twofold: First, the magnetic ordering temperature of most of the shown thin films will be lower than in strained bulk (thicker films). Second, for films below a certain thickness, the total magnetic moment will deviate significantly from a rough proportionality to the number of film layers. Note that all magnetic configurations studied here exhibit a sizable total

magnetic moment that can be measured in experiment, even those with antiparallel spin configuration. These conclusions are in line with experimental observations of Karhu *et al.*, whose measurements show a critical film thickness of about 6 nm, corresponding to approximately 95 layers, below which the ordering temperature T_C and the saturation magnetization M_{sat} drop below their respective bulk values.[3] The 5-layer structures are beyond their experimental scope. Furthermore, a significant departure of the normalized remanent magnetization from the expected behavior in helical magnets $M_r/M_{sat} \sim \sin(\zeta)/\zeta$ can be seen, where ζ is proportional to the film thickness n.[3,4] They argued that defects could be responsible for their observations. We see here that the reasons are more systematic and lie within the material's electronic structure, which is in a surprising way sensitive to quantum confinement and/or interface/surface effects.

Note that we are not making any claim here concerning the spatial direction of the spins, but just about their magnitude, relative orientation, and coupling. The magnetization will certainly lie in-plane, fixed by magnetic and shape anisotropy, and rotate helically around the [111] film normal. No remanent out-of-plane magnetization has been measured in experiments.[4]

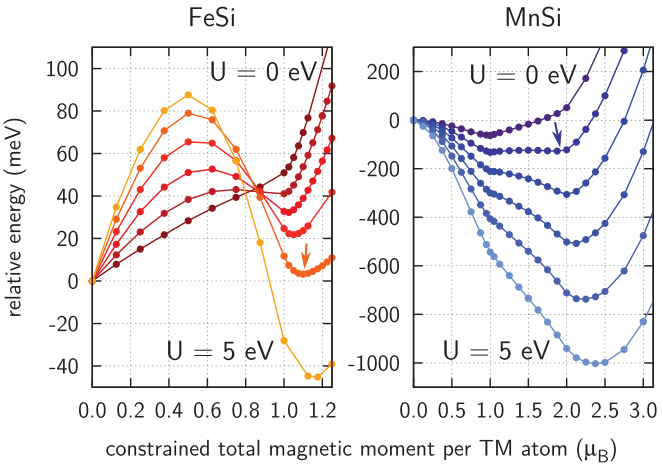

FIG. 8. (Color online) Total energy curves as a function of the constrained total magnetic moment, both per f.u., from GGA + U calculations with varying U between 0 and 5 eV in steps of 1 eV. The energy value for zero moment has been normalized to zero for each curve. A second local minimum (small arrows) can be stabilized at a higher magnetic moment by inclusion of on-site electronic correlation.

VI. CORRELATION EFFECTS IN MnSi AND FeSi: DISCUSSION AND OUTLOOK

Although we have shown throughout the previous sections that conventional GGA is capable of providing a qualitatively correct description of many of the observed phenomena, we also explored the effect of on-site electronic correlation in FeSi and MnSi. The relative stability of low-spin and high-spin states that we calculated with GGA could be sensitive to on-site correlation. For example, it was argued by Anisimov *et al.* that inclusion of a Hubbard-U term at the Fe atom could stabilize a magnetic moment of around 1 μ_B in FeSi for a value of $U >$ 4.6 eV.[53] Moreover, inclusion of on-site correlation may lead to a better description of excitations, either for comparison with spectroscopic experiments or for estimating the contributions of Stoner excitations to the magnetic susceptibility. Recent angle-resolved photoemission experiments on FeSi required an empirically determined self-energy shift to account for the correct position of the bands, but the overall DFT band structure was found to be in qualitative agreement with experiment.[47] Experiments on MnSi using x-ray absorption, photoemission, and fluorescence led to the conclusion that the Mn atoms are in a mixed valence state, thus pointing to some role of electron correlation in this material.[11] On the other hand, it was also concluded that the on-site electronic correlation in MnSi is apparently not strong enough to lead to a localization of the magnetic moments, and hence a description of MnSi as an itinerant magnet is appropriate. This view of the origin of magnetism in MnSi is also corroborated by measurements of the magnetic susceptibility: From a fit of the paramagnetic susceptibility above the Curie temperature (between 120 and 300 K) to a Curie-Weiss law, one would arrive at a magnetic moment of 2.27 μ_B, much higher than the magnetic moment of 0.4 μ_B found in saturation magnetization at low temperature.[40] Thus, the Rhodes-Wohlfarth parameter[68] of MnSi is much larger than unity, a behavior typical for an itinerant, weakly FM material. The large magnetic moment derived from the Curie-Weiss fit could point to the existence of high-spin Stoner excitations.

In order to explore these topics, we performed constrained total magnetic moment calculations for different values of U, keeping for simplicity the cell size and atomic positions fixed. We used a rotationally invariant formulation of the GGA + U scheme.[69] The results for FeSi shown in Fig. 8 reproduce quite accurately the previous results of Anisimov *et al.*,[53] in particular, the stabilization of a magnetic moment near 1 μ_B for high U values. Minor differences with respect to Ref. 53 can be attributed to the different exchange-correlation functional (GGA vs LDA) and a probably slightly different cell size.

For MnSi, a second magnetic state stabilizes around 2 μ_B already for $U \approx 1$ eV, as seen from Fig. 8. For higher values of U, the original minimum at 1 μ_B becomes unstable and the second minimum moves to higher magnetic moments. Thus, inclusion of on-site correlation does not lead to an improved agreement between the measured (via the saturation magnetization) and calculated magnetic moment in MnSi. Rather, it is likely that the deviation is due to strong quantum-dynamical spin fluctuations that reduce the moment obtained in DFT, as already noted earlier.[19,70] We conclude that the correct description of the ground state of MnSi (FeSi) is in conflict with a large value of $U > 1$ eV ($U > 4$ eV). However, the flat energy minimum observed for MnSi at $U \approx 1$ eV could be physically relevant, as it allows for energetically low-lying excitations of the Mn atom into a high-spin state, which is compatible with the large increase of the paramagnetic susceptibility near T_C.

As a side track of our work, we found that optimizing the crystal structure in the presence of U adversely affects the calculated lattice constant. With increasing U, the lattice

constant of MnSi increases also (4.58, 4.60, and 4.66 Å for 1, 2, and 3 eV, respectively), and the magnetic moments at the respective equilibrium lattice constants are even higher than those indicated in Fig. 8. Already for $U = 1$ eV, 2 μ_B is the ground state magnetic moment, at a lattice constant that is overestimated by a similar percentage as the Si lattice constant is overestimated by PBE.

Consequently, no significant increase of the total magnetic moment arises anymore if the FM calculations of Si(111)-strained bulk MnSi are performed with $U = 1$ eV. The NM-FM energy difference increases from roughly 110 meV (without U) to 276 meV, and the FIM-FM energy difference, 57 meV, is also somewhat higher than the value derived without U. This indicates a further stabilization of the high-spin FM ground state due to the on-site correlation. For FeSi, calculated with $U = 4$ eV, a higher total magnetic moment of about 1.5 μ_B is found in the FM phase, and the NM-FM energy difference raises to 300 meV. However, the FIM configuration is suddenly more stable than the FM phase, with an energy difference of 47 meV. The total magnetic moment in this FIM phase is 0.33 μ_B. (All values are given per f.u.) This and the DOS of this configuration (not shown here) still indicate a metallic character instead of a band gap at the Fermi energy. In this respect, no qualitative difference is achieved by inclusion of on-site correlation. We suggest that the magnetic properties should be measured carefully in future FeSi/Si(111) experiments to shed more light on this issue.

We conclude that for the type of electronic correlations present in FeSi and MnSi the Coulombic on-site repulsion plays only a minor role, and a GGA + U scheme is not superior to standard GGA, although it offers a possible interpretation of the high magnetic moments derived from paramagnetic susceptibility fits. For the same reason, we would not expect improvements from the use of hybrid functionals such as HSE. We rather think that it could be interesting to investigate the effect of strain in TM-Si compounds with dynamical mean-field theory. For simple bulk FeSi, this method shows a renormalization of the bands close to the Fermi energy, in agreement with experimental findings.[12] Also for MnSi, such an approach could possibly be illuminating.

VII. SUMMARY

We have discussed several 3*d* transition metal monosilicides in B20 structure and the influence of epitaxial strain on their structural, electronic, and magnetic properties based on first-principles calculations. Starting from bulk systems, we have shown that biaxial strain considerably modifies the materials properties. This is especially the case for MnSi films grown epitaxially on Si(111), where we have found a strain-induced volume expansion and an increase of the magnetic moments and of the Curie temperature in the limit of thick films, which makes the material more interesting in the field of Si-based spintronics. Additionally, this unusual behavior indicates the insufficiency of a Heisenberg-type description and points to the importance of itinerant exchange for the magnetic ordering in MnSi. Moreover, the magnetic behavior can be significantly different if the films are relatively thin (e.g., less than roughly 6 nm in experiment), as we have explicitly demonstrated for MnSi/Si(111) heterostructures. Our results agree qualitatively well with recent experimental data for MnSi, and also the structural properties of epitaxially strained FeSi are correctly described. Thus, the generalized gradient approximation for electronic exchange and correlation is capable of providing a qualitatively correct description for these materials. According to our calculations, FeSi becomes an almost half metallic ferromagnet due to strain. This is a surprising result that calls for careful experimental studies, since the Curie temperature will certainly be very small. Besides, an analysis of the orbital structure in FeSi revealed that the band gap, which can be found somewhere in the density of states for all studied B20 transition metal monosilicides, separates two opposing groups of bands with different predominant 3*d* orbital character. Finally, we have discussed the benefits and drawbacks of considering on-site electronic correlation in the framework of GGA + U.

ACKNOWLEDGMENTS

Financial support by Deutsche Forschungsgemeinschaft (DFG) within the collaborative research project SFB 491 is acknowledged. We thank Ole Krogh Andersen, Max-Planck-Institut Stuttgart, for communicating to us his unpublished results on the orbital structure of FeSi.

[1] G. A. Prinz, Science **282**, 1660 (1998).
[2] S. A. Wolf, D. D. Awschalom, R. A. Buhrman, J. M. Daughton, S. von Molnár, M. L. Roukes, A. Y. Chtchelkanova, and D. M. Treger, Science **294**, 1488 (2001).
[3] E. A. Karhu, S. Kahwaji, T. L. Monchesky, C. Parsons, M. D. Robertson, and C. Maunders, Phys. Rev. B **82**, 184417 (2010).
[4] E. A. Karhu, S. Kahwaji, M. D. Robertson, H. Fritzsche, B. J. Kirby, C. F. Majkrzak, and T. L. Monchesky, Phys. Rev. B **84**, 060404 (2011).
[5] N. A. Porter, G. L. Creeth, and C. H. Marrows, Phys. Rev. B **86**, 064423 (2012).
[6] D. Shinoda and S. Asanabe, J. Phys. Soc. Jpn. **21**, 555 (1966).
[7] H. Wu, P. Kratzer, and M. Scheffler, Phys. Rev. B **72**, 144425 (2005).
[8] H. Wu, M. Hortamani, P. Kratzer, and M. Scheffler, Phys. Rev. Lett. **92**, 237202 (2004).
[9] M. Hortamani, P. Kratzer, and M. Scheffler, Phys. Rev. B **76**, 235426 (2007).
[10] B. Geisler, P. Kratzer, T. Suzuki, T. Lutz, G. Costantini, and K. Kern, Phys. Rev. B **86**, 115428 (2012).
[11] F. Carbone, M. Zangrando, A. Brinkman, A. Nicolaou, F. Bondino, E. Magnano, A. A. Nugroho, F. Parmigiani, T. Jarlborg, and D. van der Marel, Phys. Rev. B **73**, 085114 (2006).
[12] V. V. Mazurenko, A. O. Shorikov, A. V. Lukoyanov, K. Kharlov, E. Gorelov, A. I. Lichtenstein, and V. I. Anisimov, Phys. Rev. B **81**, 125131 (2010).
[13] W. Kohn and L. J. Sham, Phys. Rev. **140**, A1133 (1965).
[14] P. Giannozzi *et al.*, J. Phys.: Condens. Matter **21**, 395502 (2009).

[15]J. P. Perdew, K. Burke, and M. Ernzerhof, Phys. Rev. Lett. **77**, 3865 (1996).
[16]D. Vanderbilt, Phys. Rev. B **41**, 7892 (1990).
[17]For VSi and NiSi we used the pseudopotentials V.pbe-sp-van.UPF and Ni.pbe-nd-rrkjus.UPF from http://www.quantum-espresso.org
[18]S. G. Louie, S. Froyen, and M. L. Cohen, Phys. Rev. B **26**, 1738 (1982).
[19]E. A. Karhu, U. K. Rößler, A. N. Bogdanov, S. Kahwaji, B. J. Kirby, H. Fritzsche, M. D. Robertson, C. F. Majkrzak, and T. L. Monchesky, Phys. Rev. B **85**, 094429 (2012).
[20]L. Bengtsson, Phys. Rev. B **59**, 12301 (1999).
[21]B. Meyer and D. Vanderbilt, Phys. Rev. B **63**, 205426 (2001).
[22]M. Methfessel and A. T. Paxton, Phys. Rev. B **40**, 3616 (1989).
[23]H. J. Monkhorst and J. D. Pack, Phys. Rev. B **13**, 5188 (1976).
[24]P. Blaha, K. Schwarz, G. K. H. Madsen, D. Kvasnicka, and J. Luitz, in *WIEN2k, an Augmented Plane Wave + Local Orbitals Program for Calculating Crystal Properties*, edited by K. Schwarz (Techn. Univ. Wien, Austria, 2001).
[25]Z. Z. Zhang, B. Partoens, K. Chang, and F. M. Peeters, Phys. Rev. B **77**, 155201 (2008).
[26]D. van der Marel, A. Damascelli, K. Schulte, and A. A. Menovsky, Physica B **224**, 138 (1998).
[27]B. Borén, Ark. Kemi, Mineral. Geol. **11A**, 1 (1933).
[28]M. Vočadlo, G. D. Price, and I. G. Wood, Acta Crystallogr. Sect. B **55**, 484 (1999).
[29]T. Jeong and W. E. Pickett, Phys. Rev. B **70**, 075114 (2004).
[30]M. Ekman and V. Ozolins, Phys. Rev. B **57**, 4419 (1998).
[31]W. Gale and T. Totemeier, eds., *Smithells Metals Reference Book*, 8th ed. (Elsevier Science, New York, 2004).
[32]O. Madelung, ed., *Landolt-Börnstein, New Series*, Vol. IV/5J (Springer, Berlin, 1998).
[33]S. Mühlbauer, B. Binz, F. Jonietz, C. Pfleiderer, A. Rosch, A. Neubauer, R. Georgii, and P. Böni, Science **323**, 915 (2009).
[34]A. Hamann, D. Lamago, T. Wolf, H. v. Löhneysen, and D. Reznik, Phys. Rev. Lett. **107**, 037207 (2011).
[35]Y. Ishikawa, K. Tajima, D. Bloch, and M. Roth, Solid State Commun. **19**, 525 (1976).
[36]P. Bak and M. H. Jensen, J. Phys. C: Solid State Phys. **13**, L881 (1980).
[37]O. Nakanishi, A. Yanase, A. Hasegawa, and M. Kataoka, Solid State Commun. **35**, 995 (1980).
[38]Y. Ishikawa and M. Arai, J. Phys. Soc. Jpn. **53**, 2726 (1984).
[39]S. V. Grigoriev, S. V. Maleyev, A. I. Okorokov, Y. O. Chetverikov, and H. Eckerlebe, Phys. Rev. B **73**, 224440 (2006).
[40]S. M. Stishov, A. E. Petrova, S. Khasanov, G. K. Panova, A. A. Shikov, J. C. Lashley, D. Wu, and T. A. Lograsso, Phys. Rev. B **76**, 052405 (2007).
[41]J. Wernick, G. Wertheim, and R. Sherwood, Mater. Res. Bull. **7**, 1431 (1972).
[42]M. Fäth, J. Aarts, A. A. Menovsky, G. J. Nieuwenhuys, and J. A. Mydosh, Phys. Rev. B **58**, 15483 (1998).
[43]S. Paschen, E. Felder, M. A. Chernikov, L. Degiorgi, H. Schwer, H. R. Ott, D. P. Young, J. L. Sarrao, and Z. Fisk, Phys. Rev. B **56**, 12916 (1997).
[44]V. Jaccarino, G. K. Wertheim, J. H. Wernick, L. R. Walker, and S. Arajs, Phys. Rev. **160**, 476 (1967).
[45]T. E. Mason, G. Aeppli, A. P. Ramirez, K. N. Clausen, C. Broholm, N. Stücheli, E. Bucher, and T. T. M. Palstra, Phys. Rev. Lett. **69**, 490 (1992).
[46]Z. Fisk, J. Sarrao, S. Cooper, P. Nyhus, G. Boebinger, A. Passner, and P. Canfield, Phys. B: Condens. Matter **223-224**, 409 (1996).
[47]M. Klein, D. Zur, D. Menzel, J. Schoenes, K. Doll, J. Röder, and F. Reinert, Phys. Rev. Lett. **101**, 046406 (2008).
[48]K. Ishizaka, T. Kiss, T. Shimojima, T. Yokoya, T. Togashi, S. Watanabe, C. Q. Zhang, C. T. Chen, Y. Onose, Y. Tokura, and S. Shin, Phys. Rev. B **72**, 233202 (2005).
[49]M. Arita, K. Shimada, Y. Takeda, M. Nakatake, H. Namatame, M. Taniguchi, H. Negishi, T. Oguchi, T. Saitoh, A. Fujimori, and T. Kanomata, Phys. Rev. B **77**, 205117 (2008).
[50]L. F. Mattheiss and D. R. Hamann, Phys. Rev. B **47**, 13114 (1993).
[51]J. M. Hopkinson and H.-Y. Kee, Phys. Rev. B **74**, 224441 (2006).
[52]O. K. Andersen (private communication).
[53]V. I. Anisimov, S. Y. Ezhov, I. S. Elfimov, I. V. Solovyev, and T. M. Rice, Phys. Rev. Lett. **76**, 1735 (1996).
[54]E. Magnano, F. Bondino, C. Cepek, F. Parmigiani, and M. C. Mozzati, Appl. Phys. Lett. **96**, 152503 (2010).
[55]H. von Känel, N. Onda, H. Sirringhaus, E. Müller-Gubler, S. Goncalves-Conto, and C. Schwarz, Appl. Surf. Sci. **70-71**, 559 (1993).
[56]K. Schwinge, C. Müller, A. Mogilatenko, J. Paggel, and P. Fumagalli, J. Appl. Phys. **97**, 103913 (2005).
[57]S. Higashi, Y. Ikedo, P. Kocan, and H. Tochihara, Appl. Phys. Lett. **93**, 013104 (2008).
[58]S. Higashi, P. Kocán, and H. Tochihara, Phys. Rev. B **79**, 205312 (2009).
[59]J. Hirvonen Grytzelius, H. M. Zhang, and L. S. O. Johansson, Phys. Rev. B **78**, 155406 (2008).
[60]J. Hirvonen Grytzelius, H. M. Zhang, and L. S. O. Johansson, Phys. Rev. B **80**, 235324 (2009).
[61]Le Thanh Vinh, J. Chevrier, and J. Derrien, Phys. Rev. B **46**, 15946 (1992).
[62]S. Picozzi, A. Continenza, and A. J. Freeman, Phys. Rev. B **66**, 094421 (2002).
[63]S. Baroni, S. de Gironcoli, A. Dal Corso, and P. Giannozzi, Rev. Mod. Phys. **73**, 515 (2001).
[64]S. V. Grigoriev, D. Chernyshov, V. A. Dyadkin, V. Dmitriev, E. V. Moskvin, D. Lamago, T. Wolf, D. Menzel, J. Schoenes, S. V. Maleyev, and H. Eckerlebe, Phys. Rev. B **81**, 012408 (2010).
[65]S. V. Grigoriev, D. Chernyshov, V. A. Dyadkin, V. Dmitriev, S. V. Maleyev, E. V. Moskvin, D. Menzel, J. Schoenes, and H. Eckerlebe, Phys. Rev. Lett. **102**, 037204 (2009).
[66]K. Reuter, C. Stampfl, and M. Scheffler, in *Handbook of Materials Modeling*, edited by D. Yip (Kluwer, Dordrecht, The Netherlands, 2004).
[67]N. Chetty and R. M. Martin, Phys. Rev. B **45**, 6089 (1992).
[68]E. Wohlfarth, J. Magn. Magn. Mater. **7**, 113 (1978).
[69]M. Cococcioni and S. de Gironcoli, Phys. Rev. B **71**, 035105 (2005).
[70]T. Moriya, *Spin Fuctuations in Itinerant Electron Magnetism* (Springer, Berlin, 1985).